ANZIAM J. 58(2016), 96–118
doi:10.1017/S1446181116000134

UNSTEADY TWO-LAYERED BLOOD FLOW THROUGH A *w*-SHAPED STENOSED ARTERY USING THE GENERALIZED OLDROYD-B FLUID MODEL

AKBAR ZAMAN✉[1], NASIR ALI[1], O. ANWAR BEG[2] and M. SAJID[1]

(Received 4 October, 2015; accepted 20 January, 2016; first published online 21 July 2016)

Abstract

A theoretical study of an unsteady two-layered blood flow through a stenosed artery is presented in this article. The geometry of a rigid stenosed artery is assumed to be *w*-shaped. The flow regime is assumed to be laminar, unsteady and uni-directional. The characteristics of blood are modelled by the generalized Oldroyd-B non-Newtonian fluid model in the core region and a Newtonian fluid model in the periphery region. The governing partial differential equations are derived for each region by using mass and momentum conservation equations. In order to facilitate numerical solutions, the derived differential equations are nondimensionalized. A well-tested explicit finite-difference method (FDM) which is forward in time and central in space is employed for the solution of a nonlinear initial boundary value problem corresponding to each region. Validation of the FDM computations is achieved with a variational finite element method algorithm. The influences of the emerging geometric and rheological parameters on axial velocity, resistance impedance and wall shear stress are displayed graphically. The instantaneous patterns of streamlines are also presented to illustrate the global behaviour of the blood flow. The simulations are relevant to haemodynamics of small blood vessels and capillary transport, wherein rheological effects are dominant.

2010 *Mathematics subject classification*: 76A05.

Keywords and phrases: unsteady two-layered flow, generalized Oldroyd-B fluid, finite-difference method, haemodynamics, stenosis, finite-element method, streamline visualization.

1. Introduction

The composition of blood is known to be a multi-component mixture of aqueous plasma, red blood cells (RBCs), white blood cells (WBCs) and a variety of lipoproteins [43]. The fact that rheological characteristics of blood influence many of the

[1]Department of Mathematics and Statistics, International Islamic University, Islamabad, 44000, Pakistan; e-mail: akbarzaman75@yahoo.com, nasir.ali@iiu.edu.pk, sajidqau2002@yahoo.com.
[2]Spray Research Group, Petroleum and Gas Engineering Division, School of Computing, Science and Engineering (CSE), University of Salford, M5 4WT, UK; e-mail: O.A.Beg@salford.ac.uk.

pathological conditions observed in the circulatory system has stimulated research in two distinct directions with regard to the constitutive modelling of blood. The first approach is more general and is founded on microcontinuum theories and emphasizes the use of additional balance laws to characterize the rheology of blood. The second approach simulates blood as a suspension and implements the use of techniques of macroscopic non-Newtonian fluid mechanics. In view of the former approach, the rheology of blood can be successfully characterized by the constitutive equations of micropolar, dipolar, couple stress and micromorphic fluid models. The latter approach allows a variety of constitutive equations to be deployed to represent the shear stress–strain behaviour of blood depending on different non-Newtonian characteristics. It is also well established that blood exhibits nonlinear properties due to the presence of RBCs, which form approximately 45% of the volume of normal human blood, under certain flow conditions. Typical non-Newtonian characteristics exhibited by blood are shear thinning, thixotropy, viscoelasticity and yield stress.

Time-independent non-Newtonian models are commonly used in the literature to capture the shear-thinning property of blood. These include the power-law model [26], Carreau model [44], Casson model [16], Walburn–Schneck model [21], Cross model [13] and Weaver model [40], to name but a few. Thixotropic and yield-stress behaviour of blood is described quite accurately by time-dependent non-Newtonian models. Some well-known time-independent thixotropic models used in the literature on blood flow are the Huang model [19], Weltman model [36], Tiu–Boger model [36] and Rosen model [9]. As emphasized by Thurston [41], the viscoelastic behaviour of blood becomes prominent at low shear rates due to aggregation of RBCs. Therefore, under pulsatile flow conditions the blood may be modelled as a viscoelastic fluid. Popular viscoelastic fluid models in haemodynamics, which are adopted to characterize blood rheology, include the Oldroyd-B fluid model, Yeleswarapu model [42], generalized Maxwell model [35] and generalized Oldroyd-B (GOB) model [3].

Significant experimental evidence also exists demonstrating that rheological properties of blood may change with variations in the diameter of the vessel. For instance, it has been observed that the measured apparent viscosity of blood decreases with reducing diameter of the blood vessel. This phenomenon is known as the Fahreaus–Lindqvist (FL) effect [15]. This effect may be due to migration of RBCs away from the wall, resulting in formation of a cell-depleted layer near the wall. Many researchers have modelled blood as a two-layered fluid to capture the FL effect. The peripheral (or cell-depleted) plasma layer is modelled as a Newtonian fluid while the core region (mixture of RBCs and plasma) is modelled as a non-Newtonian fluid. Following this approach, Majhi and Usha [25] modelled the core region using the thermodynamically robust constitutive equation of third grade fluids to capture the FL effect. Subsequently, Majhi and Nair [24] extended their previous analysis to include the effect of pulsatile conditions and body acceleration. Massoudi and Phuoc [28] analysed the blood in the core region as a modified second grade fluid to study pulsatile flow of blood in a normal artery. Recently, Sajid et al. [38] analysed the pulsatile flow of blood utilizing the constitutive equation of Oldroyd-B fluid to model the core region,

https://doi.org/10.1017/S1446181116000134 Published online by Cambridge University Press

and therein also elaborated on the effects of relaxation and retardation constants on various haemodynamic characteristics.

In the above-mentioned studies, the results are reported for a normal artery. The practical significance of these results is limited, since they do not elucidate the fluid dynamics characteristics of blood in diseased (or stenotic) arteries. This has motivated some researchers to conduct similar investigations for stenotic arteries. Ikbal et al. [20] considered the unsteady two-layered blood flow through a flexible artery under stenotic conditions, using Eringen's elegant micropolar fluid model. Sankar and Lee [39] have analysed steady flow of blood through a catheterized artery via a two-fluid model with the core region approximated as a Casson fluid and the plasma in the peripheral region as a Newtonian fluid.

Motivated in extending and improving the above studies, we propose to examine theoretically the unsteady two-layered pulsatile flow of blood through a stenosed artery. The viscoelastic and shear-thinning effects of blood are both simultaneously important in the pulsatile flow under consideration. In this context, a model which is capable of concurrently predicting the shear-thinning and viscoelastic effects may be more appropriate. The GOB model [6, 32] is quite suitable for the present flow situation, since it is able to capture shear-thinning and viscoelastic effects based on thermodynamic considerations and it permits the relaxation time to be a constant. It includes a shear-rate-dependent viscosity, and has proved effective in numerous haemodynamic (and indeed other) scenarios. The Oldroyd-B model has earlier been employed to investigate pulsatile flow of blood in a tube of infinite length and circular cross-section [33]. The results of Pontrelli [34] highlight the combined effects of the viscoelasticity and of shear-dependent viscosity. The present study also generalizes the results of Mohamed and Reddy [29] for an overlapping stenosed artery. Moreover, it includes the results of the conventional Oldroyd-B fluid, Maxwell fluid, Carreau fluid and Newtonian (Navier–Stokes) fluid as special cases. The coupled constitutive and motion equations are solved numerically using a stable, convergent, explicit finite-difference method (FDM) which is forward in time and central in space. The results of velocity obtained via this method are first validated with a variational finite-element method (FEM) and, then, the flow characteristics of blood for various models (which include Oldroyd-B, Maxwell, Carreau and Newtonian models) are compared and discussed in detail. In summary, the present article addresses the unsteady two-layer blood flow through a *w*-shaped stenosed artery with a GOB rheological fluid model. The geometry of the overlapping stenosis is carefully defined. Viscous flow characteristics of blood in a stenosed artery for Carreau, Oldroyd-B and Maxwell models are compared.

The paper is structured as follows. The flow geometry is illustrated in Section 2. The problem is modelled with appropriate assumptions in Section 3. Section 4 presents the details of the numerical procedure for solution of the developed equations with a validation of the finite-element code given in Section 5. The obtained results are discussed in Section 6. The main conclusions of the present study are summarized in Section 7.

https://doi.org/10.1017/S1446181116000134 Published online by Cambridge University Press

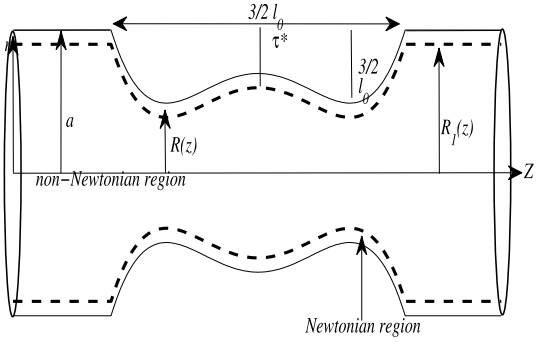

FIGURE 1. Geometry of the overlapping stenotic artery.

2. Problem description

A homogeneous incompressible two-layered fluid (blood) is assumed to be flowing through an overlapping stenosed artery of length L. A cylindrical coordinate system (r, θ, z) is employed for the current analysis. The mathematical equation describing the geometry of the stenosis and interface is given as

$$(R, R_1)(z) = \begin{cases} (a, a^*) - \dfrac{128}{5}\dfrac{(\delta^*, \tau^*)}{l_0^4}\left\{\dfrac{11}{32}l_0^3(z-d) - \dfrac{47}{48}l_0^2(z-d)^2 + l_0(z-d)^3 - \dfrac{1}{3}(z-d)^4\right\}, \\ \qquad d \le z \le d + \dfrac{3}{2}l_0, \\ (a, a^*), \quad \text{otherwise.} \end{cases}$$

In the above expression, $R(z)$ denotes the radius of the arterial segment with stenosis, δ^* is the maximum height of the stenosis, a is the constant radius of the artery in the nonstenotic region, a^* is the radius of a core region, l_0 is the length of the stenosis, d is the length of the pre-stenotic region, τ^* is the bulging of the interface and $R_1(z)$ denotes the radius of the central core layer. A schematic diagram of the nontapered artery is shown in Figure 1.

Note that (δ^*, τ^*) denote the critical heights of the two-layered stenosis appearing at two specific locations, that is,

$$z = d + \frac{9l_0}{50} \quad \text{and} \quad z = d + \frac{41l_0}{50}.$$

3. Haemodynamic model

The equations governing the blood flow are

$$U^i_{,i} = 0 \quad \text{and} \quad \rho a^i = T^{ij}_{,j}, \tag{3.1}$$

where V^i are the velocity components, ρ is the fluid density, T^{ij} are the components of the Cauchy stress tensor, "," denotes the covariant derivative and a^i are the components

https://doi.org/10.1017/S1446181116000134 Published online by Cambridge University Press

of the acceleration vector given as

$$a^i = \frac{\partial U^i}{\partial t} + U^r U^i_{,r}.$$

The constitutive law for the incompressible fluid takes the form

$$T^{ij} = -p\delta^{ij} + S^{ij},$$

in which p, δ^{ij} and S^{ij} are the pressure, identity tensor and extra stress tensor, respectively. We have delineated the arterial domain into two distinct regions: $0 \leq r \leq R_1$ (a core region) and $R_1 \leq r \leq R$ (a periphery region). For the present case, the rheology of blood in the core region is characterized by the constitutive equation of a GOB fluid, while in the periphery region it is assumed to satisfy the well-known Newtonian constitutive law. Thus, the equation for S^{ij} in the core region is [29]

$$S_{ij} + \lambda_1 \frac{DS^{ij}}{Dt} = \left[\mu(\Pi) + \mu_0\lambda_2 \frac{D}{Dt}\right] A_i^{ij}, \quad 0 \leq r \leq R_1, \tag{3.2}$$

where

$$\mu(\Pi) = \mu_\infty + (\mu_0 - \mu_\infty)[1 + \Gamma^2\Pi^2]^{(n-1)/2}.$$

In the periphery region, S^{ij} is defined as

$$S_{ij} = \mu_1 A_1^{ij}, R_1 \leq r \leq R. \tag{3.3}$$

In equations (3.2) and (3.3), μ_0 and μ_∞ are zero-shear-rate and infinite-shear-rate viscosities, respectively, Γ is the time constant, n is the power-law index, λ_1 and λ_2 are relaxation and retardation times, respectively, and A_1^{ij} are the components of the first Rivlin–Ericksen tensor given by

$$A_1^{ij} = U^i_{,j} + U^j_{,i}.$$

The second invariant of the first Rivlin–Ericksen tensor Π is defined as

$$\Pi = \sqrt{\tfrac{1}{2}(A_1^{pk} A_1^{kp})}.$$

Under mild stenotic conditions, the flow in the artery can be treated as uni-directional and unsteady. Let u_1 and u_2 denote nonvanishing axial velocity components in core and peripheral regions, respectively. From a momentum balance (3.1), the axial velocity component in the peripheral region satisfies

$$\rho_2 \frac{\partial u_2}{\partial t} = -\frac{\partial p}{\partial z} + \frac{1}{r}\frac{\partial}{\partial r}(rS^{rz}), \tag{3.4}$$

where

$$S^{rz} = \mu_1 \frac{\partial u_2}{\partial r}, \quad R_1 \leq r \leq R \tag{3.5}$$

https://doi.org/10.1017/S1446181116000134 Published online by Cambridge University Press

and ρ_2 is the fluid density in the peripheral region. Similarly, the axial velocity component in the core region satisfies

$$\rho_1 \frac{\partial u_1}{\partial t} = \frac{\partial p}{\partial z} + \frac{1}{r}\frac{\partial}{\partial r}(rS^{rz}), \tag{3.6}$$

where ρ_1 is the fluid density in the core region. In view of (3.2), S^{rz} in the core region satisfies the following equation [31]:

$$\left(1 + \lambda_1 \frac{\partial}{\partial t}\right) S_{rz} = \left[\left\{\mu_\infty + (\mu_0 - \mu_\infty)\left(1 + \gamma^2 \left|\frac{\partial u_1}{\partial r}^2\right|\right)^{(n-1)/2}\right\} + \mu_1 \lambda_2 \frac{\partial}{\partial t}\right]\frac{\partial u_1}{\partial r}, \quad 0 \le r \le R_1.$$

Since the flow is initiated by the pulsatile pressure gradient [11], we write

$$\frac{\partial p}{\partial z} = A_0\left(1 + \frac{A_1}{A_0}\cos(\omega_p t)\right).$$

Here, A_0 is the systolic, A_1 the diastolic component of the pressure gradient, $\omega_p = 2\pi f_p$ the circular frequency and f_p the pulse rate frequency. Eliminating S^{rz} between equations (3.4) and (3.6), we get the equation for the velocity components in the core region as follows:

$$\begin{aligned}\rho_1\left(\frac{\partial u_1}{\partial t} + \lambda_1 \frac{\partial^2 u_1}{\partial t^2}\right) &= A_0\left\{1 + \frac{A_1}{A_0}\cos(\omega_p t) - \lambda_1 \frac{A_1}{A_0}\sin(\omega_p t)\right\} \\ &+ \frac{\mu_0}{r}\left[\left\{\frac{\mu_\infty}{\mu_0} + \left(1 - \frac{\mu_\infty}{\mu_0}\right)\left(1 + \Gamma^2\left|\frac{\partial u_1}{\partial r}^2\right|^{(n-1)/2}\right)\right\}\frac{\partial u_1}{\partial r} + \lambda_2 \frac{\partial^2 u_1}{\partial r \partial t}\right] \\ &+ \mu_0\left[\left\{\frac{\mu_\infty}{\mu_0} + \left(1 - \frac{\mu_\infty}{\mu_0}\right)\left(1 + \Gamma^2\left|\frac{\partial u_1}{\partial r}^2\right|^{(n-1)/2}\right)\right\}\frac{\partial^2 u_1}{\partial r^2}\right. \\ &\left. + \left\{\frac{\mu_\infty}{\mu_0} + \left(1 - \frac{\mu_\infty}{\mu_0}\right)\left(1 + \Gamma^2\left|\frac{\partial u_1}{\partial r}^2\right|^{(n-1)/2}\right)\right\}\frac{\partial u_1}{\partial r} + \lambda_2 \frac{\partial^3 u_1}{\partial r^2 \partial t}\right]. \end{aligned} \tag{3.7}$$

Similarly, substitution of equations (3.5) into (3.6) yields the determining equation for u_2 as

$$\rho_2 \frac{\partial u_2}{\partial t} = A_0\left(1 + \frac{A_1}{A_0}\cos(\omega_p t)\right) + \mu_1\left(\frac{1}{r}\frac{\partial u_2}{\partial r} + \frac{\partial^2 u_2}{\partial r^2}\right), \tag{3.8}$$

where a subscript denotes differentiation with respect to the indicated variable. We introduce the following variables:

$$\bar{r} = \frac{r}{a}, \quad \bar{z} = \frac{z}{L}, \quad \bar{u}_i = \frac{u}{U_0} \quad (i = 1, 2), \quad \bar{t} = \frac{\omega_p}{2\pi}t,$$

$$U_0 = \frac{A_0 a^2}{\mu_i}, \quad \bar{p} = \frac{a^2 p}{\mu_i U_0 L} \quad (i = 1, 2),$$

$$\bar{\lambda}_1 = \frac{\lambda_1 \omega_p}{2\pi}, \quad \bar{\lambda}_2 = \frac{\lambda_2 \omega_p}{2\pi}, \quad \bar{\Gamma} = \frac{\Gamma U_0}{a}, \quad \rho^* = \frac{\rho_1}{\rho_2},$$

$$\alpha_1 = \frac{\rho_1 \omega_p a^2}{2\pi\mu_0}, \quad \alpha_2 = \frac{\rho_2 \omega_p a^2}{2\pi\mu_2} = \left(\frac{\mu^*}{\rho^*}\right)\alpha_1,$$

$$e = \frac{A_1}{A_0}, \quad B_1 = \frac{A_0 a^2}{\mu_0 U_0}, \quad \widehat{B}_1 = \frac{A_0 a^2}{\mu_1 U_0} = \mu^* B_1, \quad \gamma = \frac{\mu_\infty}{\mu_0}, \quad \beta = \frac{R_1}{a}.$$

https://doi.org/10.1017/S1446181116000134 Published online by Cambridge University Press

Making use of these variables, equations (3.7)–(3.8) can be changed to the following dimensionless forms:

$$\alpha_1\left(\frac{\partial u_1}{\partial t}+\lambda_1\frac{\partial^2 u_1}{\partial t^2}\right)=B_1\{1+e\cos(2\pi t)\}-2\lambda_1 eB_1\pi\sin(2\pi t)+\frac{1}{r}\left[\left\{\gamma+(1-\gamma)\times\left(1+\Gamma^2\left|\frac{\partial u_1}{\partial r}\right|^{2^{(n-1)/2}}\right)\right\}\frac{\partial u_1}{\partial r}+\lambda_2\frac{\partial^2 u_1}{\partial r\partial t}\right]+\left[\left\{\gamma+(1-\gamma)\times\left(1+\Gamma^2\left|\frac{\partial u_1}{\partial r}\right|^{2^{(n-1)/2}}\right)\right\}\frac{\partial^2 u_1}{\partial r^2}+\left\{\gamma+(1-\gamma)\times\left(1+\Gamma^2\left|\frac{\partial u_1}{\partial r}\right|^{2^{(n-1)/2}}\right)\right\}\frac{\partial u_1}{\partial r}+\lambda_2\frac{\partial^3 u_1}{\partial r^2\partial t}\right],\tag{3.9}$$

$$\alpha_2\frac{\partial u_2}{\partial t}=\widehat{B}_1\{1+e\cos(2\pi t)\}+\frac{1}{r}\frac{\partial u_2}{\partial r}+\mu_2\frac{\partial^2 u_2}{\partial r^2}.\tag{3.10}$$

In the preceding equations, the bar notation has been omitted for brevity. The above equations are subject to the following boundary and initial conditions:

$$u_{1r}(r,t)|_{r=0}=0,\quad u_1(r,t)|_\beta=u_2(r,t)|_\beta,\quad u_{1r}(r,t)|_\beta=u_{2r}(r,t)|_\beta,$$
$$u_2(r,t)|_{r=R}=0\quad\text{and}\quad u_1(r,0)=0.$$

The first condition represents the symmetry of velocity with respect to the central plane. The next two conditions at $r=\beta$ indicate the continuity of velocity and stresses at the interface. The penultimate condition corresponds to the well-known no-slip initiation at the wall. The last condition represents the initiation of flow from the rest state. The physical quantities of interest such as volumetric flow rate, wall shear stress (WSS) and resistance impedance in dimensionless form are, respectively,

$$Q=\int_0^\beta u_1 r\,dr+\int_\beta^1 u_2 r\,dr,\quad \tau_w=\left(\frac{\partial u_2}{\partial r}\right)_{r=R(z)}\quad\text{and}\quad \Lambda=\frac{(\partial p/\partial z)}{Q},$$

where

$$R(z)=(1,\beta)-\tfrac{128}{5}(\delta,\tau)\{\tfrac{11}{32}(z-\sigma)-\tfrac{47}{48}(z-\sigma)^2+(z-\sigma)^3-\tfrac{1}{3}(z-\sigma)^4\}$$

with $\sigma\le z\le\sigma+3/2$, $\delta=\delta^*/a$, $\tau=\tau^*/a$ and $\sigma=d/l_0$. Employing a radial coordinate transformation [23], $x=r/R(z)$, equations (3.9) and (3.10) can be transformed into the following equations, respectively:

$$\alpha_1\left(\frac{\partial u_1}{\partial t}+\lambda_1\frac{\partial^2 u_1}{\partial t^2}\right)=B_1\{1+e\cos(2\pi t)-2\lambda_1 eB_1\pi\sin(2\pi t)\}+\frac{1}{xR^2}\left[\left\{\gamma+(1-\gamma)\times\left(1+\left(\frac{\Gamma}{R}\right)^2\left|\frac{\partial u_1}{\partial x}\right|^{2^{(n-1)/2}}\right)\right\}\frac{\partial u_1}{\partial x}+\lambda_2\frac{\partial^2 u_1}{\partial x\partial t}\right]+\frac{1}{R^2}\left[\left\{\gamma+(1-\gamma)\times\left(1+\left(\frac{\Gamma}{R}\right)^2\left|\frac{\partial u_1}{\partial x}\right|^{2^{(n-1)/2}}\right)\right\}\frac{\partial^2 u_1}{\partial x^2}+\left\{\gamma+(1-\gamma)\times\left(1+\left(\frac{\Gamma}{R}\right)^2\left|\frac{\partial u_1}{\partial x}\right|^{2^{(n-1)/2}}\right)\right\}\frac{\partial u_1}{\partial x}+\lambda_2\frac{\partial^3 u_1}{\partial x^2\partial t}\right],\tag{3.11}$$

$$\alpha_2\frac{\partial u_2}{\partial t}=\widehat{B}_1\{1+e\cos(2\pi t)\}+\frac{1}{xR^2}\frac{\partial u_2}{\partial x}+\frac{1}{R^2}\frac{\partial^2 u_2}{\partial x^2}.\tag{3.12}$$

https://doi.org/10.1017/S1446181116000134 Published online by Cambridge University Press

The dimensionless initial and boundary conditions become

$$u_1'|_{x=0} = 0, \quad u_2|_{x=1} = 0, \quad u_1|_\beta = u_2|_\beta, \quad u_1'|_\beta = u_2'|_\beta, \quad u_k|_{t=0} = 0 \tag{3.13}$$

for $k = 1, 2$. Similarly, the volume flow rate, shear stress at the wall and resistance (impedance), respectively, assume the forms

$$Q = R^2\left(\int_0^\beta u_1 x\,dx + \int_\beta^1 u_2 x\,dx\right), \quad \tau_w = \frac{1}{R}\left(\frac{\partial u_2}{\partial r}\right)_{x=1} \quad \text{and} \quad \Lambda = \frac{(\partial p/\partial z)}{Q}. \tag{3.14}$$

Substituting the dimensionless form of the pressure gradient into equation (3.14),

$$\Lambda = \frac{B_1\{1 + e\cos(2\pi t)\}}{R^2(z)\left(\int_0^\beta u_1 x\,dx + \int_\beta^1 u_2 x\,dx\right)}. \tag{3.15}$$

4. Explicit finite difference method solutions

Since the parabolic system of equations (3.11) and (3.12) is not amenable to analytical solution due to its nonlinear nature, we shall employ an appropriate numerical technique for its solution. An explicit scheme which is forward in time and central in space is used [2, 17, 27]. Let $u_{k,i}^j$ denote the value of u_k $(k = 1, 2)$ at spatial node x_i and time instant t_j. In this notation, the appropriate expressions of various partial derivatives are as follows:

$$\frac{\partial u_k}{\partial x} \cong \frac{u_{k,i+1}^j - u_{k,i-1}^j}{2\Delta x} = u_{kx},$$
$$\frac{\partial^2 u_k}{\partial x^2} \cong \frac{u_{k,i+1}^j - 2u_{k,i}^j + u_{k,i-1}^j}{(\Delta x)^2} = u_{kx^2}.$$

Similarly, we approximate the time derivatives

$$\frac{\partial u_k}{\partial t} \cong \frac{u_{k,i}^{j+1} - u_{k,i}^j}{2\Delta t} = u_{kt},$$
$$\frac{\partial^2 u_{ki}}{\partial t^2} \cong \frac{u_{k,i+1}^{j+1} - 2u_{k,i}^j + u_{k,i}^{j-1}}{(\Delta t)^2} = u_{kt^2},$$
$$\frac{\partial}{\partial t}\left(\frac{\partial u_k}{\partial x}\right) \cong \frac{u_{k,i+1}^{j+1} - u_{k,i+1}^j - u_{k,i-1}^{j+1} + u_{k,i-1}^j}{2\Delta x \Delta t} = u_{ktx},$$
$$\frac{\partial}{\partial t}\left(\frac{\partial^2 u_k}{\partial x^2}\right) \cong \frac{u_{k,i+1}^{j+1} - 2u_{k,i}^{j+1} + u_{k,i-1}^{j+1} - u_{k,i+1}^j + 2u_{k,i}^j - u_{k,i-1}^j}{(\Delta x)^2 \Delta t} = u_{ktx^2}.$$

https://doi.org/10.1017/S1446181116000134 Published online by Cambridge University Press

Using the above formulae for time and spatial derivatives, equations (3.11) and (3.12) are transformed into the following finite-difference forms:

$$
\begin{aligned}
u_{1i}^{j+1} = {} & \frac{1}{1+(\lambda_1/\Delta t)}\Bigg[u_{1i}^{j}\left(1+\frac{2\lambda_1}{\Delta t}\right)-\frac{\lambda_1}{\Delta t}u_{1i}^{j-1} \\
& +\left(\frac{\Delta t}{\alpha_1}\right)B_1\{1+e\cos(2\pi t^j)-2\lambda_1 eB_1\pi\sin(2\pi t^j)\} \\
& +\frac{1}{xR^2}\Bigg[\left\{\gamma+(1-\gamma)\left(1+\left(\frac{\Gamma}{R}\right)^2|u_{1x}^2|^{(n-1)/2}\right)\right\}u_{1x}+\lambda_2 u_{1xt}\Bigg]+\frac{1}{R^2}\Bigg[\left\{\gamma+(1-\gamma)\right. \\
& \left.\times\left(1+\left(\frac{\Gamma}{R}\right)^2|u_{1x}^2|^{(n-1)/2}\right)\right\}u_{1x^2} \\
& +\left\{(1-\gamma)\frac{\partial}{\partial x}\left(1+\left(\frac{\Gamma}{R}\right)^2|u_{1x}^2|^{(n-1)/2}\right)\right\}u_{1x}+\lambda_2 u_{1tx^2}\Bigg]\Bigg], \\
u_{2i}^{j}+1 = {} & u_{2i}^{j}+1+\left(\frac{\delta t}{\alpha_2}\right)\left[\widehat{B}_1\{1+e\cos(2\pi t^j)\}+\frac{1}{xR^2}(u_{2x})+\frac{1}{R^2}u_{2x^2}\right].
\end{aligned}
$$

The finite-difference representation of the associated prescribed boundary conditions (3.13) is given by

$$
\begin{aligned}
u_i^1 &= 0 \quad \text{at } t = t_1 = 0, \\
u_{1N_c+1}^{j} &= u_{2N_c+1}^{j} \quad \text{at } x = x_{N_c+1} = \beta, \\
u_{N+1}^{k} &= 0 \quad \text{at } x = 1, \\
u_1^k &= u_2^k \quad \text{at } x = 0.
\end{aligned}
$$

The uniformly distributed discrete points in the radial direction are defined as $x_i = (i-1)\Delta x$ $(i = 1, 2, \ldots, N_c+1)$ such that $x_{N_c+1} = \beta$, and $x_i = (i-(N_c+1))\Delta x$ $(i = N_c+1, N_c+2, \ldots, N+1)$ and $x_{N+1} = 1$, where Δx is the increment in the radial direction. Similarly, we define $t_j = (j-1)\Delta t$ $(i = 1, 2, \ldots)$ as discrete time points with Δt indicating a small time increment. At a particular cross-section, the simulations are carried out for a specific value of the temporal and spatial step sizes, $\Delta t = \Delta t_1$ and $\Delta x = \Delta x_1$. Indeed, it is anticipated that for this specific choice, the numerical values of velocity may not be convergent. This claim can be verified by choosing lower values of $\Delta t = \Delta t_2(\Delta t_1)$ and $\Delta x = \Delta x_1(\Delta x_2)$, and then comparing the numerical values of velocity with the previously obtained values. Now, if the absolute difference between the corresponding numerical values is less than the prescribed tolerance, say 10^{-7}, then it can be inferred that the results are accurate up to seven decimal places for $\Delta t = \Delta t_1$ and $\Delta x = \Delta x_1$. For the present problem, an accuracy of 10^{-7} is achieved by taking $\Delta t = 0.00001$ and $\Delta x = 0.025$.

5. Validation with variational finite-element code

The results obtained via the FDM computations are also validated by the FEM. The nonlinear boundary value problem described by the coupled partial differential equations (3.11)–(3.12) under conditions (3.13) has also been solved with a variational

https://doi.org/10.1017/S1446181116000134 Published online by Cambridge University Press

FEM. The FEM has a different approach to the FDM. Numerical integration is employed rather than numerical differentiation. Owing to this and the adaptability of the FEM to complex material and geometrically nonlinear problems, the FEM remains the most popular numerical method in engineering sciences. In nonlinear biomechanics, the FEM approach has successively resolved numerous problems in diverse areas including peristaltic pumping [8], biomagnetic therapy [5], biomembrane structural stability [14], functional graded implant mechanics [18], pulsatile non-Newtonian flows [4] and respiratory fluid dynamics [30]. Pressure-gradient and time conditions (temporal) are re-defined. Following some numerical tests, mesh independence is confirmed for the present scenario with 480 line finite elements. The whole domain is therefore divided into a set of 480 line elements of equal width, each element being two-noded. Line elements are adequate, since only one spatial variable, that is, the normalized radial coordinate x, is involved. A variational form is derived for each of the transport equations (3.11)–(3.12) with the leading master variables u_1 and u_2. The numerical integration is performed over the artificial finite-element domain in terms of the normalized radial coordinates (x_e, x_{e+1}) using arbitrary test functions (W_1, W_2), which can be viewed as the variation in the master variables, following Reddy [37] and Bathe [7]. The nonlinear terms in equations (3.11)–(3.12) are easily accommodated. The finite-element form of the variational equations is achieved by appropriate substitutions, based on the approximations

$$u_1 = \sum_{j=1}^{2} u_{2j}\psi_j \quad \text{and} \quad u_2 = \sum_{j=1}^{2} u_{1j}\psi_j$$

with the weighting functions [7, 37], $W_1 = W_2 = \psi_i, i = 1, 2$. The shape (interpolation) functions for a typical line element (x_e, x_{e+1}) in the above equation are given as

$$\psi_1^{(e)} = \frac{x_{e+1} - x}{x_{e+1} - x_e}, \quad \psi_2^{(e)} = \frac{x - x_e}{x_{e+1} - x_e} \quad \text{for } x_e \le x \le x_{e+1}.$$

The matrix–vector form of the finite-element model is then generated. For details, the reader is referred to the literature [5, 8, 14], wherein comprehensive guidance is provided. This system of nonlinear algebraic equations produced after the assembly of the element equations is linearized by incorporating functions u_1 and u_2, which are assumed to be known. Boundary conditions (3.13) are also easily constructed. Following imposition of the initial (time) and boundary conditions, the matrix system is condensed and solved iteratively with a modified Householder elimination method, maintaining an accuracy of 0.0005. For extra rapid convergence, the Bathe subspace iteration procedure may also be employed [7]. Table 1 shows that very good agreement is attained between the FEM and FDM results. Confidence is therefore very high in the present FDM computations. Table 1 further provides a useful benchmark for researchers to refer to for refinements of the present investigation.

https://doi.org/10.1017/S1446181116000134 Published online by Cambridge University Press

TABLE 1. Numerical values of axial velocity at a cross-section $z = 0.79$ corresponding to the critical height of the stenosis for $\lambda_1 = 0.3, \lambda_2 = 0.1, \Gamma = 1, \delta = 0.1, t = 1.15$.

	Numerical values of axial velocity			
x	$n = 0.7$ FDM	$n = 0.7$ FEM	$n = 1$ FDM	$n = 1$ FEM
0	1.0648	1.0647	0.9079	0.9077
0.1000	1.0566	1.0564	0.8995	0.8994
0.2000	1.0276	1.0275	0.8702	0.8701
0.3000	0.9778	0.9776	0.8214	0.8212
0.4000	0.9060	0.9059	0.7535	0.7536
0.5000	0.8110	0.8109	0.6674	0.6672
0.6000	0.6920	0.6918	0.5639	0.5638
0.7000	0.5483	0.5485	0.4442	0.4441
0.8000	0.3799	0.3801	0.3096	0.3095
0.9000	0.1938	0.1939	0.1609	0.1610
1.0000	0	0	0	0

6. Results and interpretation

In this section, we are interested in establishing the response of the axial velocity, flow rate, WSS and resistance (impedance) to flow for different values of nondimensional parameters, namely the relaxation and retardation times λ_1 and λ_2, respectively, geometrical parameter β, time constant Γ and power-law parameter n. In all numerical computations, the following set of default parameters is used, following Yilmaz and Gundogdu [43]:

$$l_0 = 1, \quad B_1 = 4, \quad \beta = 0.8, \quad L = 2.5, \quad \alpha_1 = \alpha_2, \quad \mu_0 = 0.56,$$
$$\mu_\infty = 0.035, \quad \phi = 0.0, \quad e = 0.3, \quad \sigma = 0.5.$$

This data accurately corresponds to the realistic biorheological haemodynamics. Figures 2–4 demonstrate the dimensionless velocity profiles of blood at the stenotic throat of the arterial segment under study. The effects of power-law index n and time constant Γ on axial velocity are shown in Figures 2(a) and (b), respectively. Figure 2(a) shows that the magnitude of axial velocity reduces significantly by increasing n. The boost in blood viscosity with greater power-law exponent serves to decrease the shear rate and this decelerates the flow, manifesting in a reduction in velocity. On the contrary, the axial velocity of blood increases with increasing Γ (Figure 2(b)), since the delay in material response is reduced with greater time constant. In both plots, the acceleration in axial velocity with greater radial coordinate is however apparent. Figure 3 illustrates the effect of relaxation and retardation time constants on the axial velocity of blood. Figure 3(a) indicates that the magnitude of dimensionless velocity profiles at the stenotic throat of the arterial segment is a decreasing function of λ_2. Figure 3(b) reveals that the axial velocity of blood follows the converse trend with increasing λ_1. The influence of both Oldroyd-B parameters (viscoelastic) is

https://doi.org/10.1017/S1446181116000134 Published online by Cambridge University Press

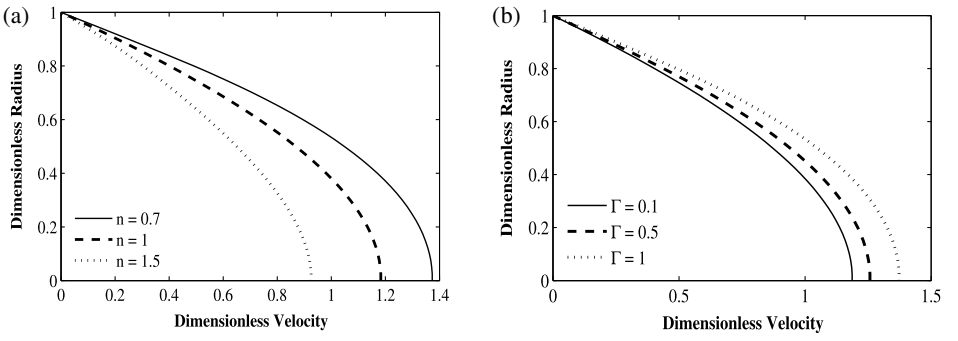

FIGURE 2. (a) Variation of velocity for different values of n ($\alpha = 0.5$, $\beta = 0.8$, $\lambda_1 = 0.3$, $\lambda_2 = 0.1$, $t = \tau_s$, $\Gamma = 1$). (b) Variation of velocity for different values of Γ ($\alpha = 0.5$, $\beta = 0.8$, $\lambda_1 = 0.3$, $\lambda_2 = 0.1$, $t = \tau_s$, $n = 0.7$).

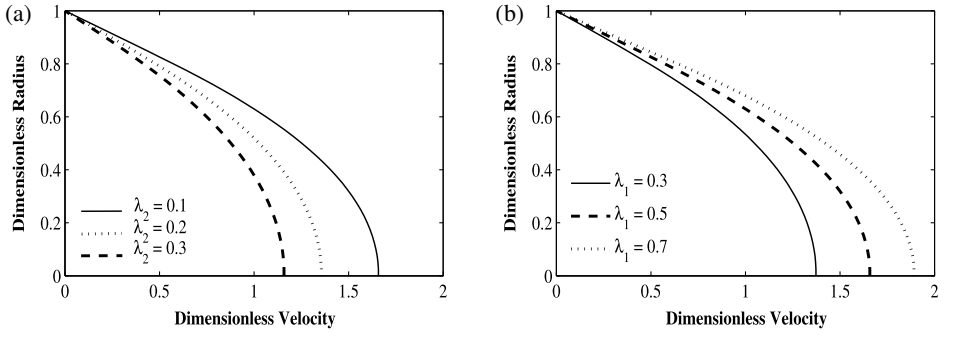

FIGURE 3. (a) Variation of velocity for different values of λ_2 ($\alpha = 0.5, \beta = 0.8, \lambda_1 = 0.5, \Gamma = 1, n = 0.7$). (b) Variation of velocity for different values of λ_1 ($\alpha = 0.5, \beta = 0.8, \lambda_2 = 0.1, \Gamma = 1, n = 0.7$).

clearly nontrivial. This emphasizes the need to include rheological characteristics in mathematical models of blood flow, and confirms the inadequacy of the Newtonian model.

The geometric parameter β can be used to investigate the effect of peripheral layer thickness on axial velocity of the flowing blood. To this end, the velocity distribution for different values of the interface position β is shown in Figure 4. It is found that the velocity decreases substantially by increasing the peripheral layer thickness. The profiles of axial velocity of blood based on different fluid models are shown in Figure 5. It is evident that the Maxwell fluid model predicts the highest values of axial velocity whilst the Newtonian fluid model predicts the least values amongst all models. Nevertheless, the non-Newtonian models all predict axial velocity magnitudes greater than the Newtonian model. The latter is therefore insufficient, and it under-predicts the flow response considerably.

The axial velocity of blood computed using Newtonian, Carreau and GOB models at $t = \tau_s$, where τ_s is the dimensionless time at which the steady-state condition has

https://doi.org/10.1017/S1446181116000134 Published online by Cambridge University Press

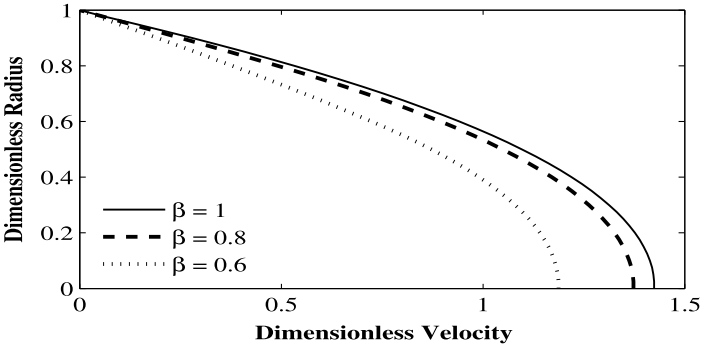

FIGURE 4. Variation of velocity with radial distance for $\alpha = 0.5, \lambda_1 = 0.5, \lambda_2 = 0.2, \Gamma = 1, t = \tau_s, n = 0.7, e = 0.3$.

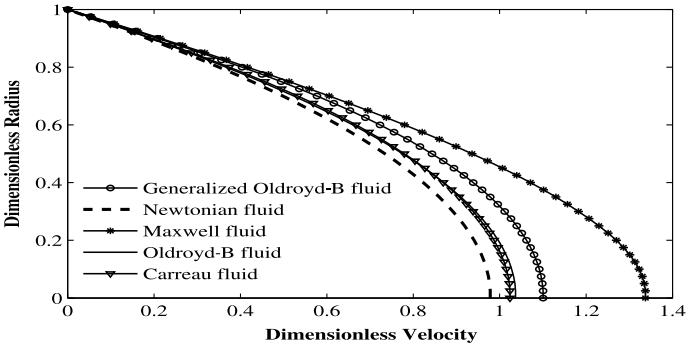

FIGURE 5. Variation of velocity with radial distance for Maxwell fluid ($\lambda_1 = 0.3, \Gamma = 0, n = 1, \lambda_2 = 0$), Oldroyd-B fluid ($\lambda_1 = 0.3, \Gamma = 0, n = 1, \lambda_2 = 0.2$), Carreau fluid ($\lambda_1 = 0, \Gamma = 0.5, n = 0.7, \lambda_2 = 0$), Newtonian fluid ($\lambda_1 = 0.0, \Gamma = 0, n = 1, \lambda_2 = 0$) and GOB fluid ($\lambda_1 = 0.3, \Gamma = 0.5, n = 0.7, \lambda_2 = 0.2$), with $\alpha = 1, t = \tau_s$.

been reached, is compared with experimental results of Bugliarello and Sevilla [10] in Figure 6. The axial velocity curves predicted by the models of Kang and Eringen [22], Akay and Kaye [1] and Chaturani and Upadhya [12] are also included in the comparison. It is observed that velocity profiles predicted by GOB and Careau models approximate the experimental data of Bugliarello and Sevilla [10] relatively closer than the other models. It is important to mention that the GOB model involves four parameters (three time constants and a power-law index) and provides greater freedom than the other models in choosing the rheological parameters to get a velocity profile closer to the experimental results. In contrast, the Newtonian model does not give any such freedom. Similarly, Maxwell and Oldroyd-B models only give the possibility to tune the elastic parameters to approximate the experimental results. Moreover, the Carreau model involves a time constant in addition to a power-law exponent and gives the possibility to use both these parameters to approximate the experimental results.

https://doi.org/10.1017/S1446181116000134 Published online by Cambridge University Press

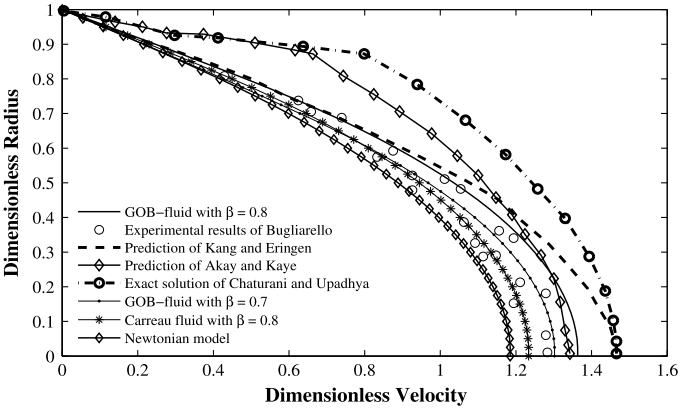

FIGURE 6. Variation of axial velocity with radial distance.

From the above discussion, we conclude that the GOB model is more flexible, and gives a number of choices to produce the axial velocity profiles closer to the experimental results. Figure 7 depicts the variation of flow rate for different values of λ_1 and λ_2 when $B = 4, e = 0.5$ and $\beta = 0.8$. Figure 7(a) indicates an elevation in flow rate as t increases from 0 to 2.1. However, after $t = 2.1$, steady-state conditions are observed to prevail, that is, flow rate becomes periodic rather than erratic. In such situations, it is found that the amplitude of the flow rate increases with increasing λ_1. Moreover, a phase shift occurs as λ_1 increases. Figure 7(b) reveals that the amplitude of the flow rate decreases with λ_2. The effect of inducing a phase shift by increasing λ_2 can also be observed in Figure 7(b). The evolution of the flow rate with time for various values of power-law index n and time constant of the Carreau model, Γ, is shown in Figure 8. It is evident from Figure 8(a) that the amplitude of oscillations in the flow rate diminishes by increasing the power-law index. On the contrary, the oscillation amplitude is found to increase with greater values of Γ (Figure 8(b)). The profiles of the flow rate corresponding to different fluid models are compared in Figure 9. Similar to velocity plots, here we observe that amongst all models, the Maxwell model predicts higher values of flow rate. The values of the flow rate predicted by the Newtonian model are the lowest computed. It is, however, important to highlight that some of the values of the flow rate predicted by the Maxwell model after achieving a steady state in the systolic phase are zero or negative, and thus might be unrealistic.

Figure 10 shows the variation of WSS in a cycle of oscillation for different values of λ_1 and λ_2 with $\beta = 0.8$. This figure indicates that the magnitude of the wall shear stress increases by increasing λ_1 (Figure 10(a)), while it is suppressed by increasing λ_2. Moreover, note that in Figure 11, the magnitude of the wall shear increases with an increase in the magnitude of the time constant Γ. The longitudinal impedance Λ of the artery is calculated using equation (3.15) and its variation during a flow cycle for different values of λ_1 and Γ with $e = 0.3$ and $\beta = 0.8$ is illustrated in Figure 12. It is observed that these profiles follow the opposite trend as compared to the flow-

https://doi.org/10.1017/S1446181116000134 Published online by Cambridge University Press

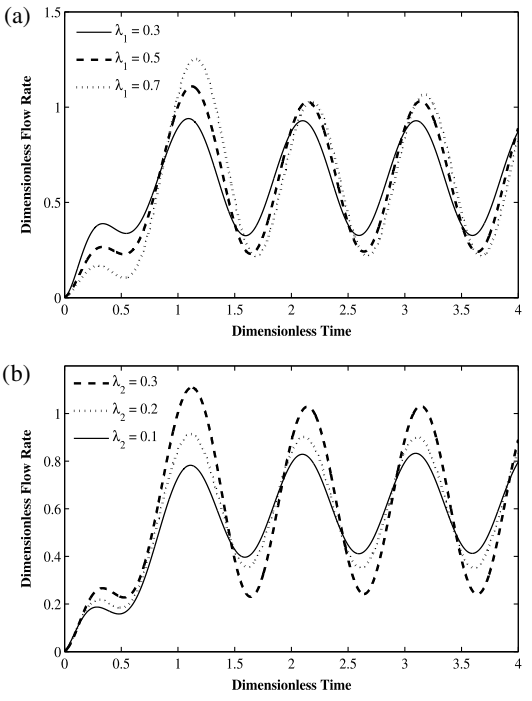

FIGURE 7. (a) Time series of flow rate for different values of λ_1 ($\alpha = 0.5, \beta = 0.8, \lambda_2 = 0.1, \Gamma = 1, n = 0.7$). (b) Time series of flow rate for different values of λ_2 ($\alpha = 0.5, \beta = 0.8, \lambda_1 = 0.5, \Gamma = 1, n = 0.7$).

rate profiles. In fact, it is found that the magnitude of resistance to flow increases with an increase in λ_1 whereas it exhibits the converse behaviour with increasing Γ. The impedance curves for different fluid models are compared in Figure 13. From this figure, it can be deduced that the impedance is minimized for a GOB fluid, whereas it is maximized for a conventional Oldroyd-B fluid. The impedance curve corresponding to the Maxwell model contains infinite jumps and, therefore, it is not shown here. These infinite jumps are the consequence of zero flow rate predicted by the Maxwell model as shown in Figure 9. Evidently, the Maxwell model has serious shortcomings limiting its applicability in haemodynamics.

The instantaneous blood flow patterns for different values of the emerging parameters are compared in Figure 14. Figure 14(a) shows the flow pattern for specific values of Γ, λ_1 and λ_2. This panel confirms the appearance of a circulating bolus of fluid in the stenotic region. It is evident from Figure 14(b) that both size and circulation of bolus decrease by increasing λ_1 from 0.5 to 0.7.

A comparison of Figure 14(a) and (c) discloses that both the size and circulation of the bolus are reduced by increasing λ_2 from 0.1 to 0.3. The effects of Γ on a circulating bolus of fluid can be observed by comparing Figure 14(a) and (d). Observe that the strength of the circulating region decreases by increasing Γ. The relative

https://doi.org/10.1017/S1446181116000134 Published online by Cambridge University Press

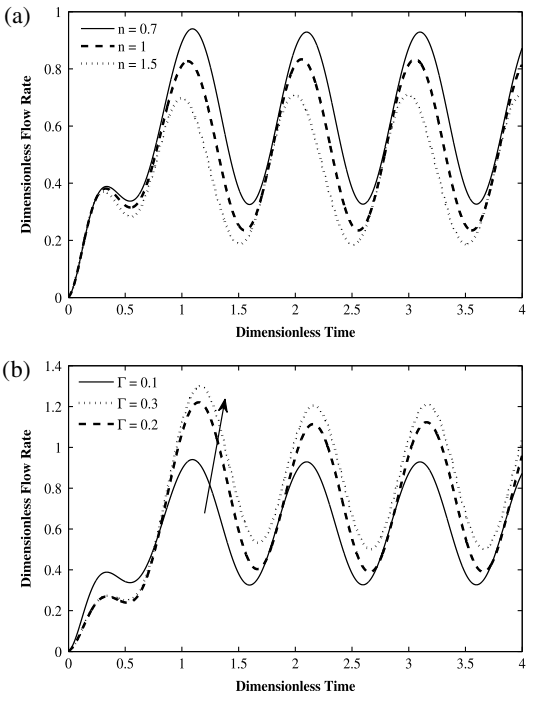

FIGURE 8. (a) Time series of flow rate for different values of n ($\alpha = 0.5$, $\beta = 0.8, \lambda_2 = 0.1, \Gamma = 1, \lambda_1 = 0.5$). (b) Time series of flow rate for different values of Γ ($\alpha = 0.5$, $\beta = 0.8, \lambda_1 = 0.5, \lambda_2 = 0.1, n = 0.7$).

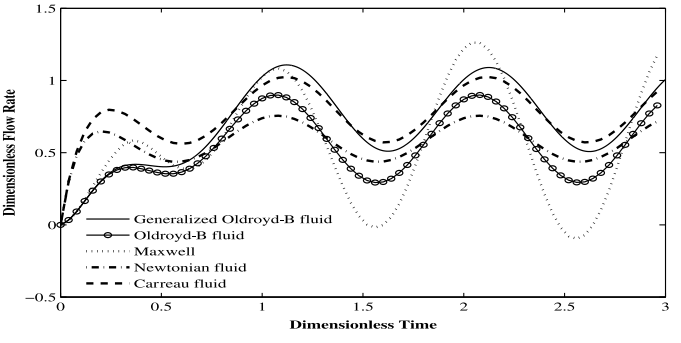

FIGURE 9. Time series of flow rate for Maxwell fluid ($\lambda_1 = 0.3, \Gamma = 0, n = 1, \lambda_2 = 0$), Oldroyd-B fluid ($\lambda_1 = 0.3, \Gamma = 0, n = 1, \lambda_2 = 0.2$), Carreau fluid ($\lambda_1 = 0, \Gamma = 0.5, n = 0.7, \lambda_2 = 0$), Newtonian fluid ($\lambda_1 = 0.0, \Gamma = 0, n = 1, \lambda_2 = 0$) and GOB fluid ($\lambda_1 = 0.3, \Gamma = 0.5, n = 0.7, \lambda_2 = 0.2$), with $\alpha = 1, t = \tau_s$.

flow patterns of blood predicted by the different rheological models can be seen by comparing Figure 14(a) with Figure 14(e)–(h). Figure 14(a) shows the instantaneous streamlines of blood flow based on the GOB model. It is noted through the comparison of Figure 14(a) with Figure 14(e) that the strength of the recirculating zone (size and

https://doi.org/10.1017/S1446181116000134 Published online by Cambridge University Press

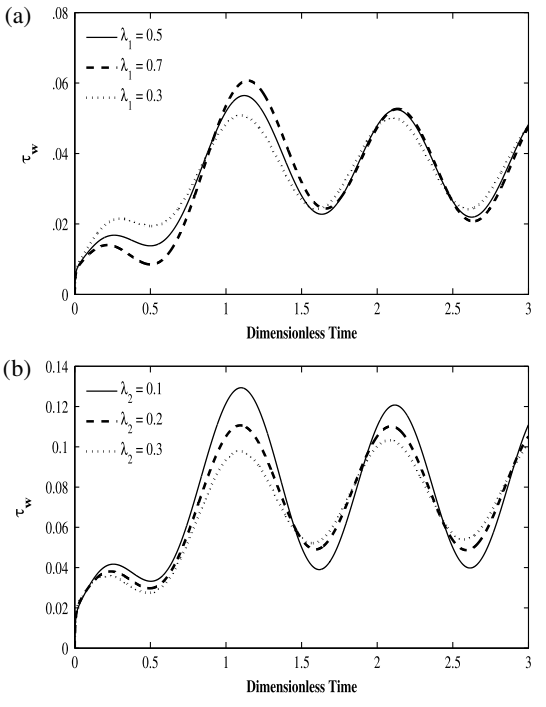

FIGURE 10. (a) Time series of WSS for λ_1 ($\alpha = 0.5$, $\beta = 0.8, \lambda_2 = 0.1, \Gamma = 1, n = 0.7$). (b) Time series of WSS for λ_2 ($\alpha = 0.5$, $\beta = 0.8, \lambda_1 = 0.5, \Gamma = 1, n = 0.7$).

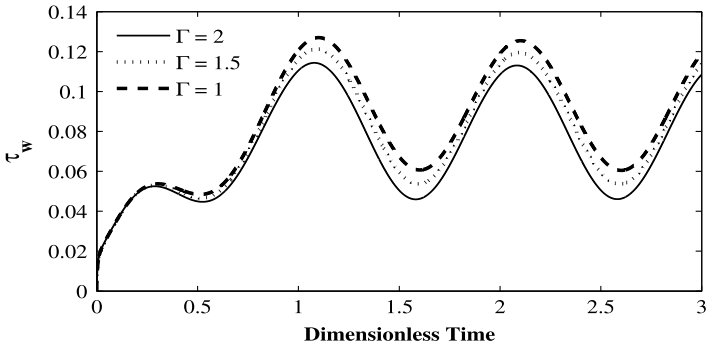

FIGURE 11. Time series of WSS for Γ ($\alpha = 0.5$, $\beta = 0.8, \lambda_2 = 0.1, \lambda_1 = 0.5, n = 0.7$).

circulation of a trapped bolus of fluid) appearing in the stenotic region decreases from the GOB fluid case to the Newtonian fluid case. Similarly, the other fluid models also predict a decrease in the size and circulation of a trapped bolus of fluid in comparison with the GOB model.

Now, at the end, we would like to comment on the significance of key results in the light of the above discussion. It is quite apparent that the axial velocity of blood

https://doi.org/10.1017/S1446181116000134 Published online by Cambridge University Press

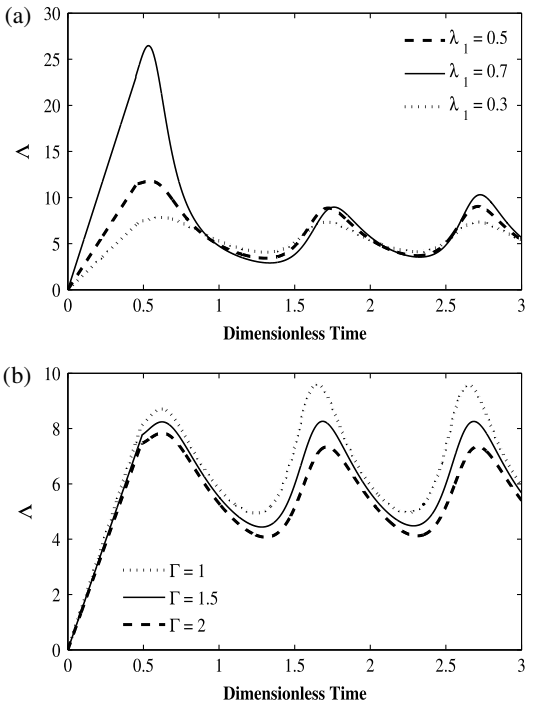

FIGURE 12. (a) Impedance plotted against time for λ_1 ($\alpha = 0.5$, $\beta = 0.8, \lambda_2 = 0.1, \Gamma = 1, n = 0.7$). (b) Impedance plotted against time for Γ ($\alpha = 0.5$, $\beta = 0.8, \lambda_1 = 0.5, \lambda_2 = 0.2, n = 0.7$).

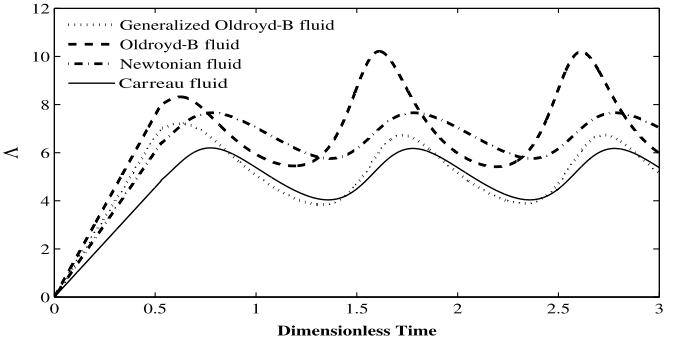

FIGURE 13. Time series of impedance for Oldroyd-B fluid ($\lambda_1 = 0.5, \Gamma = 1, n = 1, \lambda_2 = 0.2$), Carreau fluid ($\lambda_1 = 0, \Gamma = 1, n = 0.7, \lambda_2 = 0$), Newtonian fluid ($\lambda_1 = 0.0, \Gamma = 0, n = 1, \lambda_2 = 0$) and GOB fluid ($\lambda_1 = 0.5, \Gamma = 1, n = 0.7, \lambda_2 = 0.2$), with $\alpha = 1, t = \tau_s$.

diminishes significantly at the stenotic throat of the arterial segment. From Figures 2 to 4, we conclude that this decrease in the axial velocity may be controlled by tuning the rheological properties of the blood. The Newtonian model does not take into account

https://doi.org/10.1017/S1446181116000134 Published online by Cambridge University Press

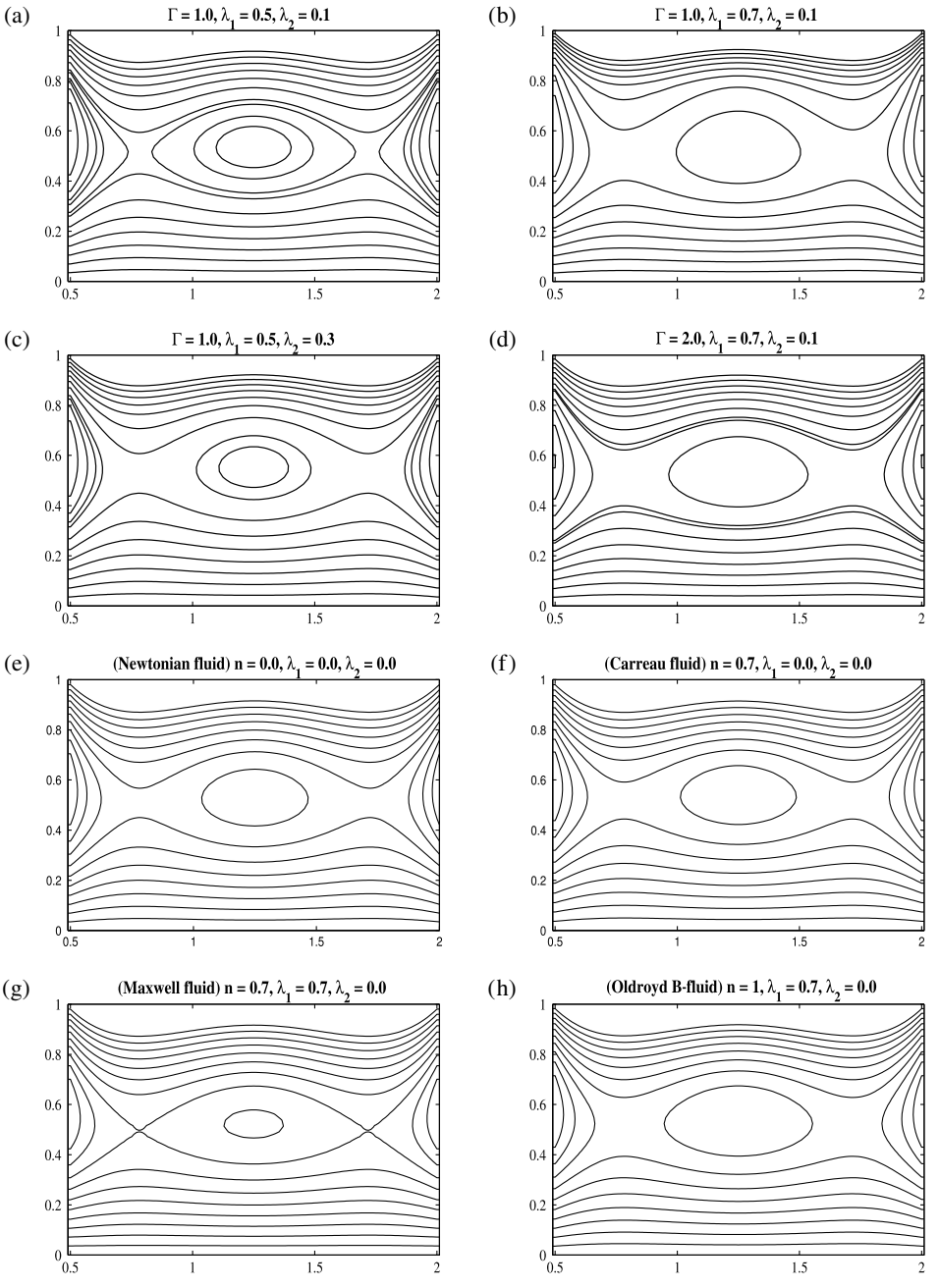

FIGURE 14. Flow patterns with the following set of values: $\alpha = 0.5$, $\beta = 0.8, \delta = 0.1, t = 0.4, e = 0.3$.

https://doi.org/10.1017/S1446181116000134 Published online by Cambridge University Press

the rheological characteristics of blood and, therefore, it is not able to predict any such remedy. In contrast, the non-Newtonian GOB model presents a number of options to tackle the situations. It allows us to tune the shear-thinning and viscoelastic properties of the blood to avoid the deceleration of blood flow at the stenotic throat.

The impedance or resistance to flow over the whole arterial segment also deteriorates due to the presence of the overlapping stenosis. The deterioration can be controlled by tuning the rheology of the blood, a solution which cannot be predicted using the Newtonian model in the modelling of blood flow through stenotic arteries. In contrast, the GOB model suggests the possibility to modulate the mechanical properties of blood, namely, its shear-thinning and viscoelastic properties, to control the deterioration in the impedance.

The instantaneous streamline patterns of blood over the whole arterial segment also reveal interesting results. A circulating bolus of blood can be readily identified in the overlapping region through all these plots. The strength of such recirculating region is strongly dependent on the rheological properties of the blood. The stronger recirculating vortices may trigger the rupturing of the overlapping region. Here again the Newtonian model does not present any solution to this problem of clinical significance. In contrast, the GOB model suggests the possibility to tune the rheology of the blood in order to avoid the undesirable process of rupturing.

7. Concluding remarks

A two-layered mathematical model has been developed for a pulsatile flow of blood through a *w*-shaped stenosed artery, using a GOB fluid model in the core region and a Newtonian model in the peripheral region. The analysis is based on the solution of a nonlinear partial differential equation corresponding to each region. Assuming the continuity of velocity at the interface and no-slip conditions, the governing equations are solved in each region by employing a finite-difference technique. Verification of the accuracy of FDM solutions is confirmed with a FEM. It is found that the resistance to flow (impedance), axial velocity, flow rate and wall shear stress are greatly affected by the rheological parameters featured in the GOB model. The flow characteristics of blood computed by applying different non-Newtonian models can also be compared through the simulation procedure documented herein. The present computations have identified that the Maxwell model predicts the highest magnitude of axial velocity amongst all other models, including the Newtonian model. The magnitude of axial velocity is the least for the Newtonian model. In the steady-state situation, the magnitude of the flow rate is highest for the GOB model and least for the conventional Oldroyd-B model. It is also observed that the flow rate computed using the Maxwell model becomes negative at certain time instants belonging to the systolic phase. Such negative values of flow rate predicted by the Maxwell model are unrealistic, as they are indicative of back flow. The impedance (resistance to flow) predicted by the GOB model is the lowest whereas it is the highest for the conventional Oldroyd-B model. The recirculating zone appears in the stenotic region for all non-Newtonian models

https://doi.org/10.1017/S1446181116000134 Published online by Cambridge University Press

including the GOB model. However, its strength is greatest in the case of the GOB model and weakest for the Maxwell model. The analysis presented here also highlights the effect of peripheral layer thickness on axial velocity of the blood. Additionally, the computations show that axial velocity significantly decreases with an increase in the peripheral layer thickness. The present study has ignored curvature of the blood vessel and also elastic wall properties. These are also key aspects of haemodynamics and will be addressed in future investigations.

Acknowledgements

The authors are grateful to the reviewer for his/her judicious comments, which have improved the present investigation. The first author is grateful to the Higher Education Commission (HEC) for financial assistance.

References

[1] G. Akay and A. Kaye, "Numerical solution of time dependent stratified two-phase flow of micropolar fluids and its application to flow of blood through fine capillaries", *Internat. J. Engrg. Sci.* **23** (1985) 265–276; doi:10.1016/0020-7225(85)0047-3.

[2] N. Ali, A. Zaman and M. Sajid, "Unsteady blood flow through a tapered stenotic artery using Sisko model", *Comput. Fluids* **101** (2014) 42–49; doi:10.1016/j.compfluid.2014.05.030.

[3] M. Anand and K. R. Rajagopal, "A shear-thinning viscoelastic fluid model for describing the flow of blood", *Int. J. Cardiovasc. Med. Sci.* **4** (2004) 59–68; https://www.cs.cmu.edu/~sangria/publications/MAKRR2004.pdf.

[4] O. Anwar Beg, T. A. Beg, R. Bhargava, S. Rawat and D. Tripathi, "Finite element study of pulsatile magneto-hemodynamic non-Newtonian flow and drug diffusion in a porous medium channel", *J. Mech. Med. Biol.* **12** (2012) 1250081.1; doi:10.1142/S0219519412500819.

[5] O. Anwar Beg, R. Bhargava, Sughanda, S. Rawat, H. S. Takhar and T. A. Beg, "Computational simulation of biomagnetic micropolar blood flow in porous (tissue) medium", in: *5th World Conf. Biomechanics, Munich, Germany* (2006).

[6] N. Arada and A. Sequeira, "Steady flows of shear-dependent Oldroyd-B fluids around an obstacle", *J. Math. Fluid Mech.* **7** (2005) 451–483; doi:10.1007/s00021-004-0133-7.

[7] K. J. Bathe, *Finite element procedures* (Prentice-Hall, Upper Saddle River, NJ, 1996).

[8] R. Bhargava, S. Sharma, H. S. Takhar, T. A. Beg, O. Anwar Beg and T. K. Hung, "Peristaltic pumping of micropolar fluid in porous channel – model for stenosed arteries", *J. Biomech.* **39** (2006) S649–S650; doi:10.1016/S0021-9290(06)85707-6.

[9] D. B. Braun and M. R. Rosen, *Rheology modifiers handbook: practical use and application* (William Andrew Publishers, Norwich, NY, 2000).

[10] G. Bugliarello and J. Sevilla, "Velocity distribution and other characteristics of steady and pulsatile blood flow in fine glass tubes", *Biorheology* **7** (1970) 85–107; http://www.ncbi.nlm.nih.gov/pubmed/5484335.

[11] A. C. Burton, *Physiology and biophysics of the circulation, introductory text* (Year Book Medical Publishers, Chicago, IL, 1966).

[12] P. Chaturani and V. S. Upadhya, "On micropolar fluid model for blood flow through narrow tubes", *Biorheology* **16** (1979) 419–428; http://www.ncbi.nlm.nih.gov/pubmed/534765.

[13] Y. I. Cho and K. R. Kensey, "Effects of the non-Newtonian viscosity of blood on hemodynamics of diseased arterial flows: part 1, steady flows", *Biorheology* **28** (1991) 241–262; http://www.ncbi.nlm.nih.gov/pubmed/1932716.

[14] J. L. Curiel Sosa, O. Anwar Beg and J. M. Liebana Murillo, "Finite element analysis of structural instability using a switching implicit–explicit technique", *Int. J. Comput. Methods Eng. Sci. Mech.* **14** (2013) 452–464; doi:10.1080/15502287.2013.784383.

[15] R. Fahraeus and T. Lindqvist, "The viscosity of blood in narrow capillary tubes", *Amer. J. Physiol.* **96** (1931) 562–568; doi:10.1161/01.RES.22.1.28.
[16] Y. C. Fung, *Biomechanics: mechanical properties of living tissues* (McGraw-Hill, New York, 1993).
[17] K. A. Hoffmann and S. T. Chiang, *Computational fluid dynamics*, 4th edn, (Engineering Education System, Wichita, KS, 2000).
[18] M. S. A. Hourai, A. Tounsi and O. Anwar Beg, "Thermoelastic bending analysis of functionally graded material sandwich plates using a new higher order shear and normal deformation theory", *Int. J. Mech. Sci.* **76** (2013) 102–111; doi:10.1016/j.ijmecsci.2013.09.004.
[19] C. R. Huang, W. D. Pan, H. Q. Chen and A. L. Copley, "Thixotropic properties of whole blood from healthy human subjects", *Biorheology* **24** (1987) 795–801; http://www.ncbi.nlm.nih.gov/pubmed/3502773.
[20] M. A. Ikbal, S. Chakravarty and P. K. Mandal, "Two-layered micropolar fluid flow through stenosed artery: effect of peripheral layer thickness", *Comput. Math. Appl.* **230** (2009) 243–259; doi:10.1016/j.camwa.2009.07.023.
[21] B. M. Johnston, P. R. Johnston, S. Corney and D. Kilpatrick, "Non-Newtonian blood flow in human right coronary arteries: steady state simulations", *J. Biomech.* **37** (2004) 709–720; doi:10.1016/j.jbiomech.2003.09.016.
[22] C. K. Kang and A. C. Eringen, "The effect of microstructure on the rheological properties of blood", *Bull. Math. Biol.* **38** (1976) 135–158; doi:10.1016/S0092-8240(76)80030-4.
[23] S. C. Ling and H. B. Atabek, "A nonlinear analysis of pulsatile flow in arteries", *J. Fluid Mech.* **55** (1972) 493–511; doi:10.1017/S0022112072001971.
[24] S. N. Majhi and V. R. Nair, "Pulsatile flow of third grade fluids under body acceleration – modeling blood flow", *Internat. J. Engrg. Sci.* **32** (1994) 839–846; doi:10.1016/0020-7225(94)90064-7.
[25] S. N. Majhi and L. Usha, "Modeling the Fahraeus–Lindqvist effect through fluids of differential type", *Internat. J. Engrg. Sci.* **26** (1988) 503–508; doi:10.1016/0020-7225(88)90008-0.
[26] P. K. Mandal, "An unsteady analysis of non-Newtonian blood through tapered arteries with a stenosis", *Int. J. Non-Linear Mech.* **40** (2005) 151–164; doi:10.1016/j.ijnonlinmec.2004.07.007.
[27] P. K. Mandal, S. Chakravarty, A. Mandal and N. Amin, "Effect of body acceleration on unsteady pulsatile flow of non-Newtonian fluid through a stenosed artery", *Appl. Math. Comput.* **189** (2007) 766–779; doi:10.1016/j.amc.2006.11.139.
[28] M. Massoudi and T. X. Phuoc, "Pulsatile flow of a blood using second grade fluid model", *Comput. Math. Appl.* **16** (2007) 199–211; doi:10.1016/j.camwa.2007.07.018.
[29] H. B. H. Mohamed and B. D. Reddy, "Some properties of models for generalized Oldroyd-B fluids", *Internat. J. Engrg. Sci.* **48** (2010) 1470–1480; doi:10.1016/j.ijengsci.2010.09.014.
[30] P. Nithiarasu, O. Hassan, K. Morgan, N. P. Weatherill, C. Fielder, H. Whittet, P. Ebden and K. R. Lewis, "Steady flow through a realistic human upper airway geometry", *Int. J. Numer. Methods Fluids* **57** (2008) 631–651; doi:10.1002/fld.1805.
[31] J. G. Oldroyd, "On the formulation of rheological equations of state", *Proc. R. Soc. Lond.* A **200** (1950) 523–541; doi:10.1098/rspa.1950.0035.
[32] M. Pires and A. Sequeira, "Flows of generalized Oldroyd-B fluids in curved pipes", *Prog. Nonlinear Differential Equations Appl.* **80** (2011) 21–43; doi:10.1007/978-3-0348-0075-4-2.
[33] G. Pontrelli, "Pulsatile blood flow in a pipe", *Comput. Fluids* **27** (1998) 367–380; doi:10.1016/S0045-7930(97)00041-8.
[34] G. Pontrelli, "Blood flow through a circular pipe with an impulsive pressure gradient", *Math. Models Methods Appl. Sci.* **10** (2000) 187–202; doi:10.1142/S0218202500000124.
[35] K. R. Rajagopal and A. R. Srinivasa, "A thermodynamic frame work for rate type fluid models", *J. Non-Newtonian Fluid Mech.* **88** (2000) 207–227; doi:10.1016/S0377-0257(99)00023-3.
[36] M. A. Rao, *Rheology of fluids and semisolid foods: principles and applications* (Springer, New York, 2007) 1–481; doi:10.1007/978-0-387-70930-7.
[37] J. N. Reddy, *An introduction to the finite element method* (McGraw-Hill, New York, 1985).

[38] M. Sajid, A. Zaman, N. Ali and A. M. Siddiqui, "Pulsatile flow of blood in a vessel using an Oldroyd-B fluid", *Int. J. Nonlinear Sci. Numer. Simul.* **16** (2015) 197–206; doi:10.1515/ijnsns-2013-0133.

[39] D. S. Sankar and U. Lee, "Two-fluid non-linear model for flow in catheterized blood vessels", *Int. J. Non-Linear Mech.* **43** (2008) 622–631; doi:10.1016/j.ijnonlinmec.2008.02.007.

[40] Y. Sugiura, "A method for analyzing non Newtonian blood viscosity data in low shear rates", *Biorheology* **25** (1988) 107–112; http://www.ncbi.nlm.nih.gov/pubmed/3196806.

[41] G. B. Thurston, "Rheological parameters for the viscosity, viscoelasticity, and thixotropy of blood", *Biorheology* **16** (1979) 149–162; http://www.ncbi.nlm.nih.gov/pubmed/508925.

[42] K. K. Yeleswarapu, "Evaluation of continuum models for characterizing the constitutive behavior of blood", Ph.D. Dissertation, University of Pittsburgh, PA, 1996.

[43] F. Yilmaz and M. Y. Gundogdu, "A critical review on blood flow in large arteries; relevance to blood rheology, viscosity models, and physiologic conditions", *Korea–Australia Rheol. J.* **20** (2008) 197–211;
http://citeseerx.ist.psu.edu/viewdoc/download?doi=10.1.1.462.7926&rep=rep1&type=pdf.

[44] A. Zaman, N. Ali, M. Sajid and T. Hayat, "Effects of unsteadiness and non-Newtonian rheology on blood flow through a tapered time-variant stenotic artery", *AIP Adv.* **5** (2015) 037129; doi:10.1063/1.4916043.